BIOMIMETICS

Avian eye–inspired perovskite artificial vision system for foveated and multispectral imaging

Jinhong Park[1,2]†, Min Seok Kim[3]†, Joonsoo Kim[1,2], Sehui Chang[3], Mincheol Lee[1,2,4], Gil Ju Lee[5], Young Min Song[3,6]*, Dae-Hyeong Kim[1,2,7]*

Avian eyes have deep central foveae as a result of extensive evolution. Deep foveae efficiently refract incident light, creating a magnified image of the target object and making it easier to track object motion. These features are essential for detecting and tracking remote objects in dynamic environments. Furthermore, avian eyes respond to a wide spectrum of light, including visible and ultraviolet light, allowing them to efficiently distinguish the target object from complex backgrounds. Despite notable advances in artificial vision systems that mimic animal vision, the exceptional object detection and targeting capabilities of avian eyes via foveated and multispectral imaging remain underexplored. Here, we present an artificial vision system that capitalizes on these aspects of avian vision. We introduce an artificial fovea and vertically stacked perovskite photodetector arrays whose designs were optimized by theoretical simulations for the demonstration of foveated and multispectral imaging. The artificial vision system successfully identifies colored and mixed-color objects and detects remote objects through foveated imaging. The potential for use in uncrewed aerial vehicles that need to detect, track, and recognize distant targets in dynamic environments is also discussed. Our avian eye–inspired perovskite artificial vision system marks a notable advance in bioinspired artificial visions.

INTRODUCTION

Bioinspired artificial vision research has yielded a multitude of unconventional imaging systems that model structural and functional characteristics of the diverse eyes in nature (*1*–*5*). These artificial visions have shown fascinating performances and potential, particularly beneficial for next-generation mobile robotics. For example, human eye–inspired curved image sensor arrays have received great attention because of their ability to generate high-quality images with low optical aberrations, even with a single lens (*6*–*15*). Analogously, imaging devices inspired by the distinctive visual capabilities of aquatic species—including fish, cuttlefish, and crabs—have been noted (*16*–*18*). These systems have exhibited broad field of view (FoV) (*19*–*21*), profound depth of field (*22*), high light sensitivity (*23*, *24*), polarized imaging capability (*25*, *26*), and amphibious vision (*17*). Compound eyes found in insects have prompted the development of cameras offering expansive FoV, nearly infinite depth of field, and high sensitivity to motion (*19*, *22*, *27*, *28*). Despite these advances, the extraordinary object detection and targeting abilities of avian eyes (*29*–*33*), specifically foveated and multispectral imaging abilities (*29*, *30*, *32*–*35*), have yet to be mimicked effectively.

As a result of countless years of evolution, avian eyes have unique ocular structures and visual functions (Fig. 1A) (*29*–*35*). In contrast to the shallow central foveae found in human eyes, certain bird species—such as raptors, swallows, and terns—have deep central foveae (*30*–*32*). This deep fovea refracts incident light to a great extent (*30*–*32*), and the region of the highest cone density lies within the fovea (Fig. 1B) (*30*, *36*). This foveated vision offers dual benefits, including magnification of the target object and simple tracking of its motion (*32*). Therefore, raptors can effectively spot, target, and track remote objects in dynamic environments (Fig. 1C and fig. S1A) (*31*). Furthermore, avian eyes have four cone types that respond to ultraviolet (UV) light and visible [red, green, blue (R, G, B)] light (Fig. 1D) (*34*–*38*). Because UV light scatters strongly on the surface of target objects (*35*), birds can gather rich information about the target objects and efficiently distinguish them from intricate backgrounds (Fig. 1, C to E, and fig. S1B) (*35*, *37*).

Foveated vision, a characteristic feature of avian eyes, is illustrated in Fig. 1 (F and G). The deep central foveae of avian eyes allow magnification of a small section of the retinal image, unlike shallow human eye foveae, which cannot provide such magnification because of their flat centers (Fig. 1F) (*30*). Central foveae are especially deep and pointed in large diurnal raptors and smaller birds that require sharp vision for hunting prey and detecting predators (*39*). Avian eyes also gather visual data with uneven spatial resolutions across their FoV because of variations in the cone density (*36*, *39*). Raptors' foveal cone densities are twice those of the human eye (*40*–*42*). This avian vision yields a magnified and high-resolution image in the foveal region while maintaining a broader FoV with a relatively lower resolution in the peripheral region (Fig. 1G). The sensitivity to motion of a target object is high at the boundary between the foveal and peripheral regions because of the variation in image magnification and resolution (Fig. 1H) (*31*–*33*).

Drawing from these remarkable avian vision capabilities, we present an artificial vision system for foveated and multispectral imaging, which consists of an artificial fovea and a vertically stacked multispectral image sensor. Optical simulations were used to optimize the artificial fovea's design and pinpoint the spatial pixel distribution within the photodetector arrays. To achieve multispectral imaging, four perovskite

[1]Center for Nanoparticle Research, Institute for Basic Science (IBS), Seoul 08826, Republic of Korea. [2]School of Chemical and Biological Engineering, Institute of Chemical Processes, Seoul National University, Seoul 08826, Republic of Korea. [3]School of Electrical Engineering and Computer Science, Gwangju Institute of Science and Technology (GIST), Gwangju 61005, Republic of Korea. [4]Electro-Medical Equipment Research Division, Korea Electrotechnology Research Institute (KERI), Ansan 15588, Republic of Korea. [5]Department of Electronics Engineering, Pusan National University, Busan 46241, Republic of Korea. [6]Artificial Intelligence (AI) Graduate School, GIST, Gwangju 61005, Republic of Korea. [7]Department of Materials Science and Engineering, Seoul National University, Seoul 08826, Republic of Korea.
*Corresponding author. Email: dkim98@snu.ac.kr (D.-H.K.); ymsong@gist.ac.kr (Y.M.S.)
†These authors contributed equally to this work.

photodetector arrays with different bandgaps (ranging between 1.73 and 3.05 eV for R, G, B, and UV) were vertically stacked in an aligned manner through transfer-printing integration. Subsequently, we combined the multispectral image sensor with the artificial fovea to construct the avian eye–inspired artificial vision system. We used this artificial vision system to demonstrate the foveated and multispectral imaging. The system could identify colored and mixed-color objects without additional color filters and could obtain a magnified view of a distant object through foveated imaging. This innovative vision system holds potential for use in mobile robotics, such as uncrewed aerial vehicles, which require detecting, tracking, and recognizing far-off targets with high precision in dynamic environments (fig. S1, C and D).

RESULTS

Design and characterization of the artificial fovea

Avian eyes, particularly those of raptors, have evolved to recognize and track distant objects, a vital skill for their hunting habits (*36*,

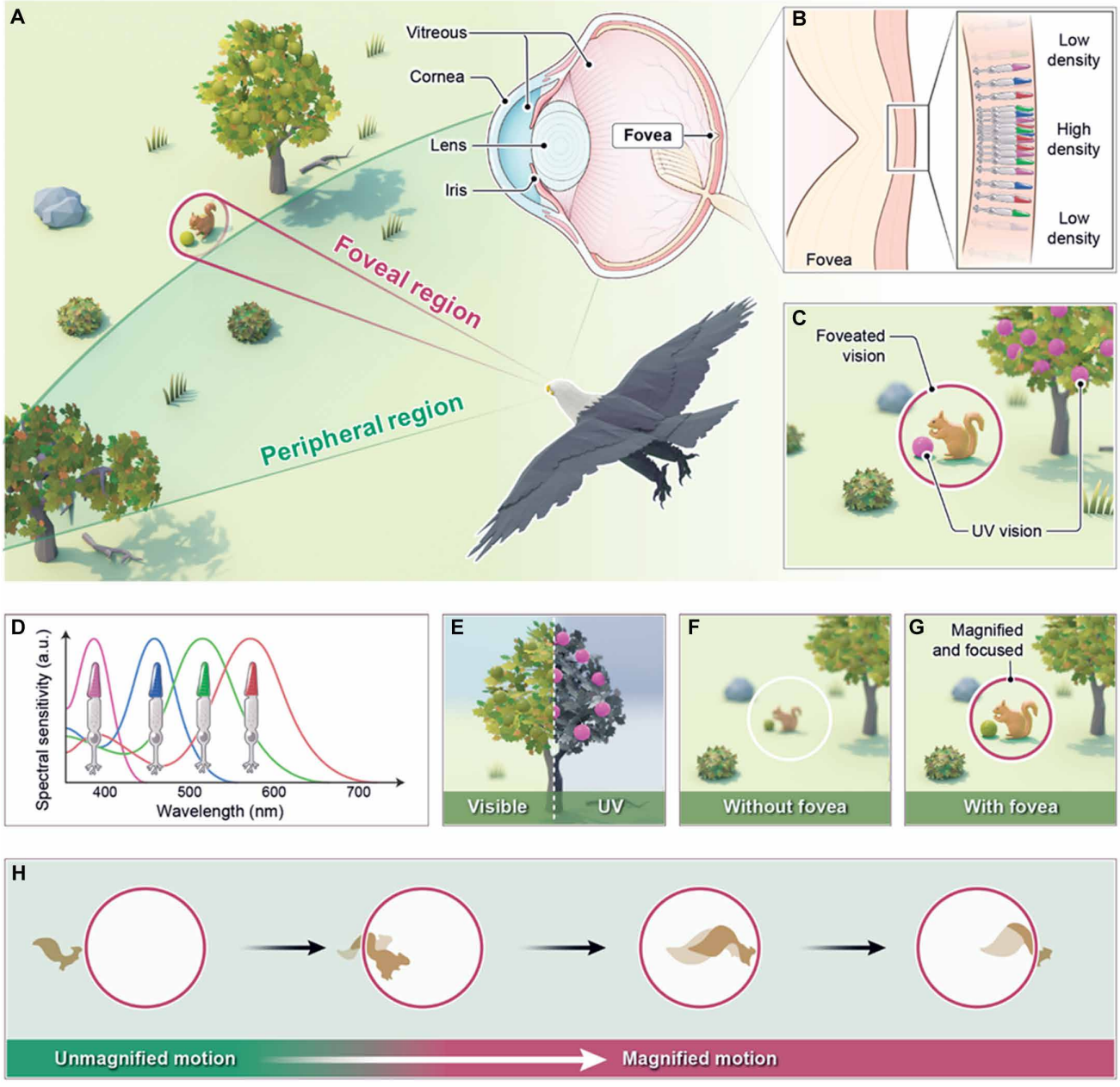

Fig. 1. Structural and functional features of avian eyes. (**A**) Schematic illustration showing the visual ecology of birds. (**B**) Magnified schematic illustration of the deep fovea in the retina. Four types of cones are arranged at different intervals under the deep fovea. (**C**) Schematic illustration of avian vision with its key features: foveated and multispectral vision. (**D**) Spectral sensitivity of cones in avian eyes. (**E**) Schematic illustrations showing RGB and UV vision. (**F** and **G**) Schematic illustrations showing images formed in the retina without (F) and with (G) fovea. With the fovea, the image of a squirrel is magnified and focused by the fovea. (**H**) Optical simulation demonstrating the principle of detecting the motion of objects through foveated vision.

37, *39*, *42*). Such capabilities are primarily a result of the geometrical and optical properties within the foveal pit (*31*–*33*). An illustration of this phenomenon is demonstrated in Fig. 2A, which presents an optical microscope image of a retinal cross section of a peregrine falcon (*Falco peregrinus*) through its central fovea (*36*). The refraction of light rays at the interface between the central fovea and vitreous humor enables the magnification of the image. The deep fovea's slope not only magnifies the image but also facilitates motion detection.

We endeavored to develop an artificial fovea by replicating the natural fovea of the avian eye. The fovea shape was strategically designed with a Gaussian profile to ensure uninterrupted magnification without blind spots or image overlap. Alternative profiles, such as cone and sphere shapes, can accompany these issues (fig. S2). The cross-sectional view of the resultant artificial fovea is shown in Fig. 2B. Its fabrication process is detailed in Materials and Methods and fig. S3. This design can be easily integrated into existing optical systems, promoting the advance of foveated imaging techniques.

Figure 2C exhibits a schematic illustration of the artificial fovea module consisting of focusing lenses and the artificial fovea. The artificial fovea's dimensions (width and depth) governed the degree of magnification (fig. S4, A to D). Further, the fovea's position and thickness influenced the focal length of the artificial fovea module (fig. S4, E to G). The artificial fovea offered different magnification levels depending on the incident ray's field angle, as shown in the ray-tracing simulation (Fig. 2D).

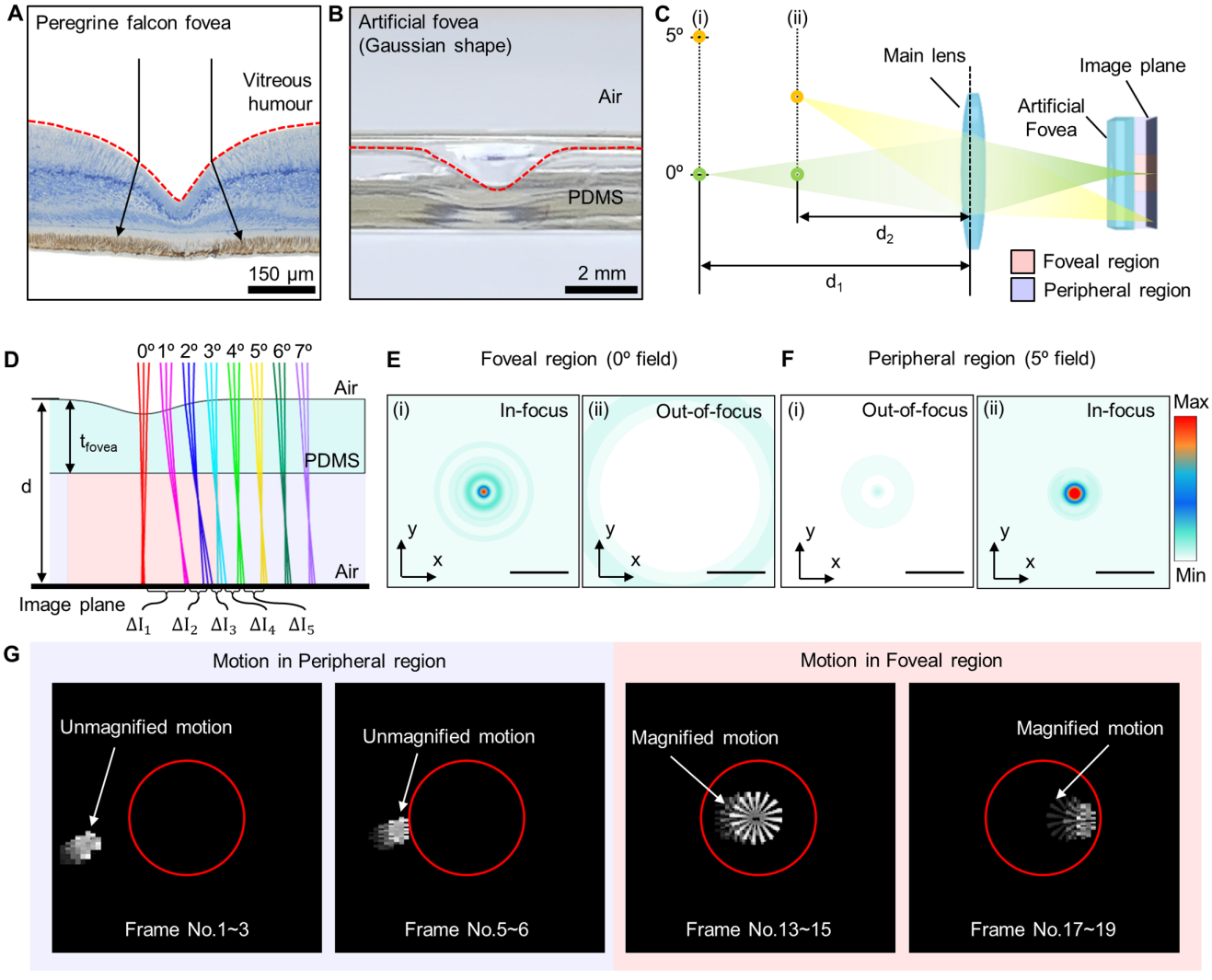

Fig. 2. Optical simulation of the artificial fovea module for foveated imaging. (**A**) Cross-sectional optical microscope image of the central fovea in a peregrine falcon's retina. The image is adapted with permission from (*36*). (**B**) Optical camera image of a cross-sectional view of the artificial fovea. (**C**) Schematic illustration of the artificial fovea module. (**D**) Ray-tracing simulation of the artificial fovea. From 0° to 2° of the field angle, corresponding to the foveal region, the incident light is refracted by the slope of the artificial fovea. The equidistant field angles from the object planes result in pixel spacings (ΔI_1, ΔI_2, ΔI_3, ΔI_4, and ΔI_5) in the image plane. (**E** and **F**) Optical simulation results showing the change in RMS spot radius with different object distance (distance between the object plane and main lens) in the foveal region (E) and peripheral region (F) of the artificial fovea module. The object distances are (i) 300 mm and (ii) 200 mm. Scale bars, 50 μm. (**G**) Image simulation results showing the difference in motion in the two regions. Siemens star object is magnified and focused by the artificial fovea in the foveal region.

Another advantage of avian vision is the geometrically foveal slope feature, a characteristic attributed to its geometrical optic structure dictated by Snell's law. This unique configuration allows birds to simultaneously focus on both near and distant objects (*32*). The artificial fovea module effectively implemented the foveal vision function observed in birds. Figure 2 (E and F) shows optical simulation results for the artificial fovea, which show changes in the root mean square (RMS) spot radius at various object distances. The artificial fovea focused on objects at different distances depending on the region (fig. S5). The foveal region with slopes sharpened distant objects (Fig. 2E), whereas the peripheral region lacking the slopes focused on closer objects (Fig. 2F).

In addition, the magnification variance between the foveal and peripheral regions enabled the detection of the target object's motion. This optical function was confirmed through image simulations. As displayed in Fig. 2G, the gear object moved from the peripheral region to the foveal region. Overlaying three frames via image processing allowed the visualization of the motion. In the peripheral region, the object remained unmagnified, resulting in a blurred image with minimal motion disparity between frames. However, as the object traversed the boundary from the peripheral region to the foveal region, the artificial fovea magnified and focused the object's image in a similar way to a zoom lens, increasing motion differences between frames and providing a sharply focused image. This image differentiation between the two regions enabled the efficient detection of the target object's motion.

Vertically stacked perovskite photodetectors with controlled bandgaps

Traditional imaging devices require the placement of Bayer color filters on a square grid photodetector to differentiate RGB (*43*). However, the demosaicing process required to reconstruct the color image in the Bayer pattern can introduce artifacts such as moiré patterns and jaggies (*44*). Various algorithms have been deployed to eradicate these artifacts (*45*, *46*), yet the pixel density limitation (imposed by the need to divide the entire pixel array into diverse color categories) remains a major setback. To circumvent this issue and replicate avian eye color perception through multispectral imaging, we implemented a vertically stacked structure of R, G, B, and UV perovskite photodetector arrays to achieve selective absorption of target wavelengths without color filters (Fig. 3A).

The perovskite layers, deposited through solvent engineering (*47*), underwent bandgap tuning by compositional substitution. Optical absorption and photoluminescence (PL) spectra of the perovskite layers are displayed in fig. S6 (A to D). The PL emission peaks corresponded to the absorption onset, implying that the principal PL emission source was the bandgap transition rather than sub-bandgap and trap sites (fig. S6, A to D) (*48*). The optical bandgaps of the quadruplet, extracted from Tauc plots, are shown in fig. S6 (E to H). In addition, strong diffraction peaks in the x-ray diffraction (XRD) spectra show the highly crystalline property of the perovskite layers (fig. S6, I to L) (*49*, *50*).

The perovskite layer thickness was strategically determined through optical and chemical modifications to completely absorb photons with higher energies than the bandgap energy, thereby preventing their transmission to the underlying perovskite photodetectors. Optical simulations, alongside the ellipsometer-based measurements of optical constants (extinction coefficient and refractive index) of each layer, were used to ascertain the minimum thickness required for each perovskite layer (fig. S7A). Once the thickness of each layer exceeds the corresponding minimum values (380, 600, 600, and 620 nm for UV, B, G and R, respectively), each perovskite layer can absorb about 95% of light with wavelengths beneath its cutoff wavelength (400, 480, 560, and 700 nm for UV, B, G, and R, respectively) (Fig. 3B and fig. S7B). The simulation results were verified through the transmittance measurements of the perovskite layers. Thick perovskite layers prepared with high precursor concentrations have negligible optical transmittance in the energy region exceeding the bandgap energy, whereas thin perovskite layers prepared with low precursor concentrations (0.4, 0.8, and 1.2 M) cannot completely absorb light (fig. S7, C and D) (*51*). The surface roughness of perovskite layers does not affect the absorbance (fig. S7, E and F).

On the basis of these optimized perovskite layers, photodetector arrays were fabricated and then vertically stacked through a transfer printing process to fabricate a multispectral image sensor (figs. S8 and S9) (*51*–*55*). Further details are documented in Supplementary Methods (see the "Fabrication process of a photodetector array" and "Transfer printing process for fabrication of multispectral image sensor" sections). A scanning electron microscopy–based cross-sectional view of the multispectral image sensor is described in Fig. 3C, portraying photodetectors for specific spectrum ranges in the multispectral image sensor, akin to avian eye cones (Fig. 1D versus Fig. 3D). The transient photoresponses of the multispectral image sensor to pulsed lights also show that each photodetector is responsive solely to the target wavelength (Fig. 3E).

Further characterizations of the multispectral image sensor included the measurement of on/off currents (Fig. 3F), whose ratios are appropriate for multispectral imaging. The illumination intensity–dependent photocurrent and responsivity follow a quasi-linear power-law relationship (*8*), as shown in fig. S10 (A to D). Current-voltage (*I*-*V*) curves under various illumination conditions are shown in fig. S10 (E to H). The photoconductor-type perovskite photodetectors exhibit symmetrical *I*-*V* curve shapes across positive and negative bias regions. Response time and stability data, exhibited in fig. S11, demonstrate photoswitching characteristics (Fig. 3E). Relatively poor operation stability of UV detectors can be further improved through the material optimization (*56*).

Pixel density variation of the multispectral image sensor for foveated vision

An exploded view of the integrated multispectral image sensor and optical microscope images of an individual pixel during its integration by the sequential transfer printing process are shown in Fig. 4 (A and B) respectively. The pixels were distributed with different intervals (Fig. 4C). Foveated imaging necessitates superior resolution in the foveal region, which is complemented by a comparatively reduced resolution in the peripheral region. Consequently, the foveal region emerges as the ideal area for precise object detection and recognition, whereas the peripheral region, offering a broad FoV, is apt for scanning the broader environment. This foveated vision allows for a more effective allocation of computational resources by prioritizing image processing in the region of interest (*57*, *58*). In alignment with this, the 8 pixels by 8 pixels in the arrays were configured with varying interpixel distances in the foveal and peripheral regions (Fig. 4, D and E).

To authenticate the effect of such pixel distributions on the imaging performance, optical simulations for flower images were conducted by altering the pixel distributions while maintaining a constant overall

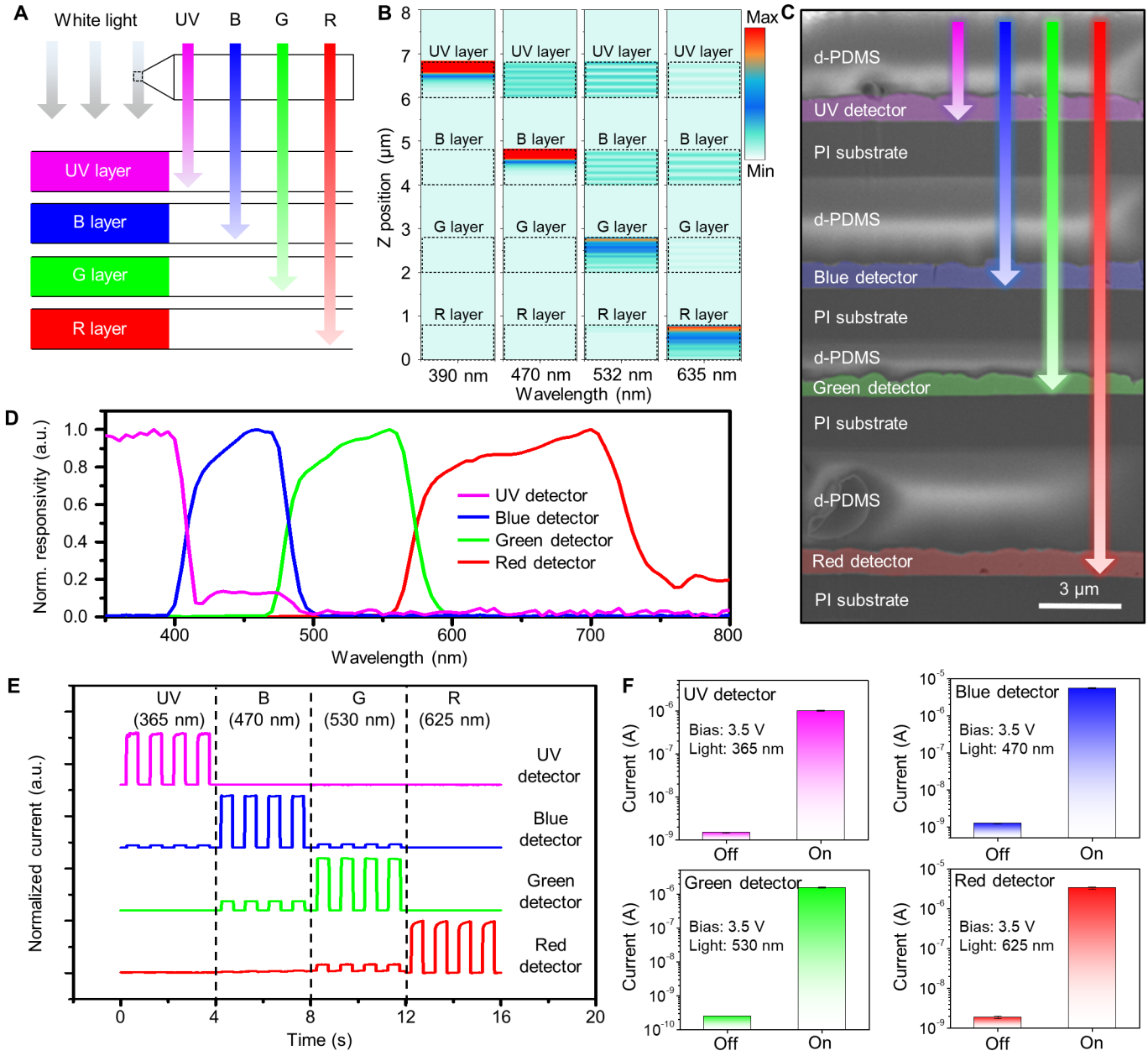

Fig. 3. Optimization of individual pixels in the multispectral image sensor for color detection without color filters. (**A**) Schematic illustration of vertically stacked perovskite layers for color detection without color filters. (**B**) Optical simulation results of vertically stacked perovskite layers. Optical simulations were performed at four wavelengths (390, 470, 532, and 635 nm). (**C**) False-colored cross-sectional SEM image of an individual pixel in the multispectral image sensor. (**D**) Normalized responsivity of an individual pixel under different wavelengths. (**E**) Transient photoresponse of an individual pixel under different wavelengths. (**F**) On/off currents of an individual pixel in the multispectral image sensor. The on current was measured under the illumination of the target wavelength with a light intensity of 40 mW/cm^2. Error bars represent the SE of 10 individual pixels.

pixel density (Fig. 4, F and G). A nonuniform pixel density (foveated density), characterized by high density at the center and lower density at the periphery, yielded discernible flower images at the center, but the peripheral region displayed blurred, low-resolution mosaic patterns (Fig. 4F). On the other hand, a uniform pixel density granted moderate resolution across the entire image. However, it did not offer the sharpness in the central flower image that the foveated imaging approach did (Fig. 4G).

Foveated and multispectral imaging with the avian eye–inspired artificial vision

For the foveated and multispectral imaging demonstration, a measurement setup consisting of target objects, a main lens, an artificial fovea, and a multispectral image sensor was designed and built as shown in Fig. 5A and fig. S12 (A to C). Detailed descriptions regarding the imaging demonstration procedures can be found in Materials and Methods.

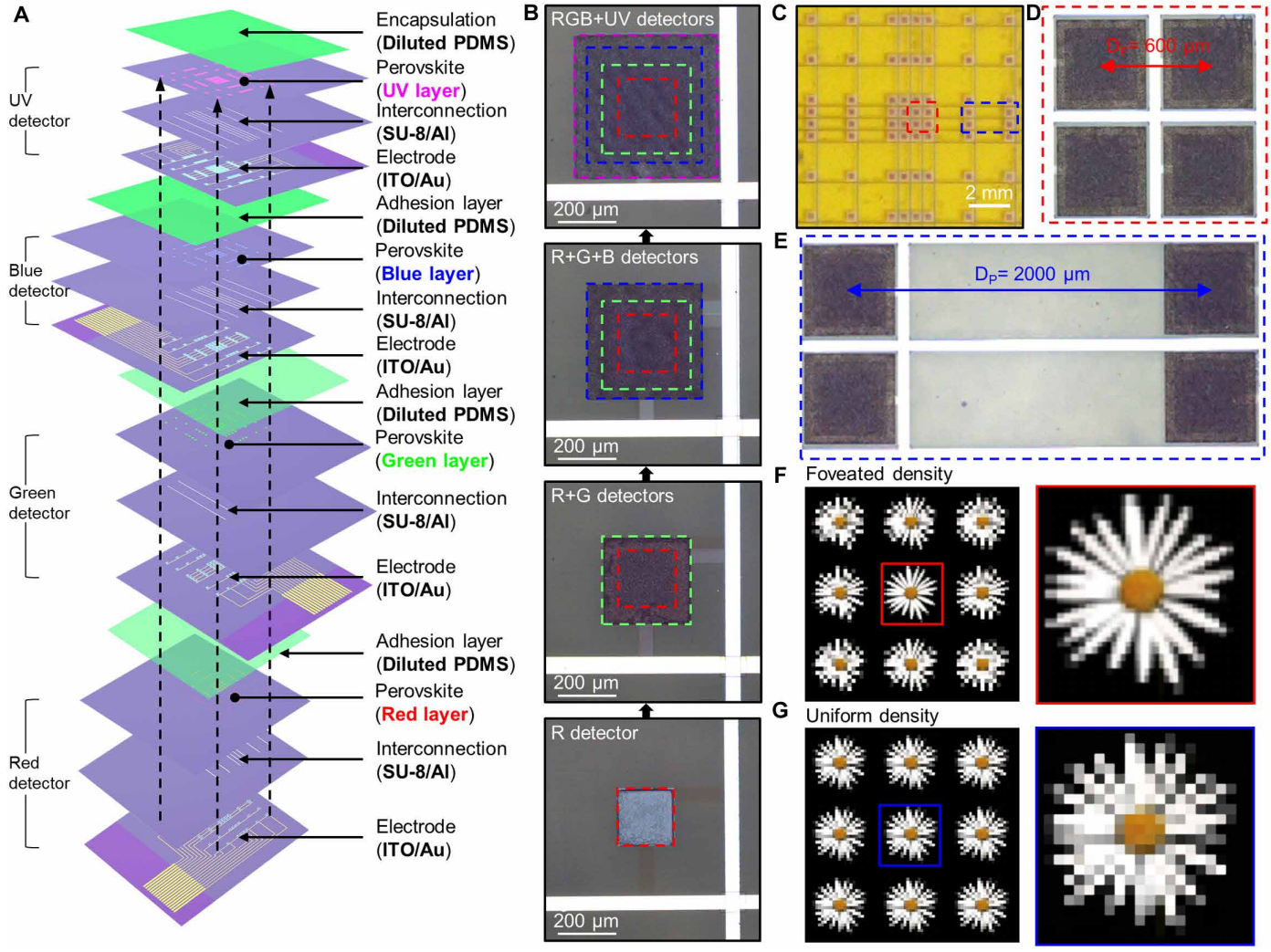

Fig. 4. Detailed structure of the multispectral image sensor. (**A**) Exploded view of the multispectral image sensor showing each layer. (**B**) Optical microscope images of an individual pixel that show sequential stacking of each photodetector array. (**C**) Optical camera image of 8 pixels by 8 pixels of the multispectral image sensor. (**D** and **E**) Optical microscope images of pixels in the foveal region [red box in (C)] (D) and peripheral region [blue box in (C)] (E). D_F and D_P represent the distance between each pixel in the foveal region and peripheral region, respectively. (**F** and **G**) Optical simulation results showing the difference in the image according to the pixel arrangement: foveated density (F) and uniform density (G).

The potential for the foveated and multispectral imaging was demonstrated using four objects. Three objects (triangle, square, and circle, colored as R, G, and B, respectively) were positioned in the peripheral region (object distance: 200 mm), whereas a star-shape object, emitting both white and UV light, was placed in the foveal region (object distance: 300 mm) (Fig. 5A). Because the focal length of the main lens was 200 mm, the three objects located within the peripheral region displayed clear and well-focused images regardless of the artificial fovea (fig. S12, D and E). However, the distant star object was out of focus in the multispectral image sensor without the artificial fovea (fig. S12D). On the other hand, in the avian eye–inspired perovskite artificial vision system (multispectral image sensor with the artificial fovea), a sharp and magnified star image was formed by the artificial fovea, although the star object was located farther than the focal length of the main lens (Fig. 5B and fig. S12E). In addition, even when the target object was partially obscured by the surrounding object, the avian eye–inspired perovskite artificial vision system provided a magnified and well-focused image of the target object in the foveal region (fig. S13).

The simulation results of the artificial fovea module for motion detection were experimentally verified through pseudo-motion detection imaging (Fig. 2G and fig. S14). The motion of the object was implemented by moving the light-emitting diode (LED)–mounted object on the optical rail system at 5-mm intervals per frame (fig. S14A). When objects entered the foveal region, the images of the objects were magnified and brought into focus (fig. S14B). In addition, the motion difference between each frame (distance between red dots in fig. S14C) in the foveal region became much larger than the motion difference in the peripheral region, although the object moved the same distance of 5 mm in both regions. These results are consistent with the simulation results in Fig. 2G.

The influence of the pixel distribution on the imaging performance was also experimentally verified (Fig. 5C). In agreement with

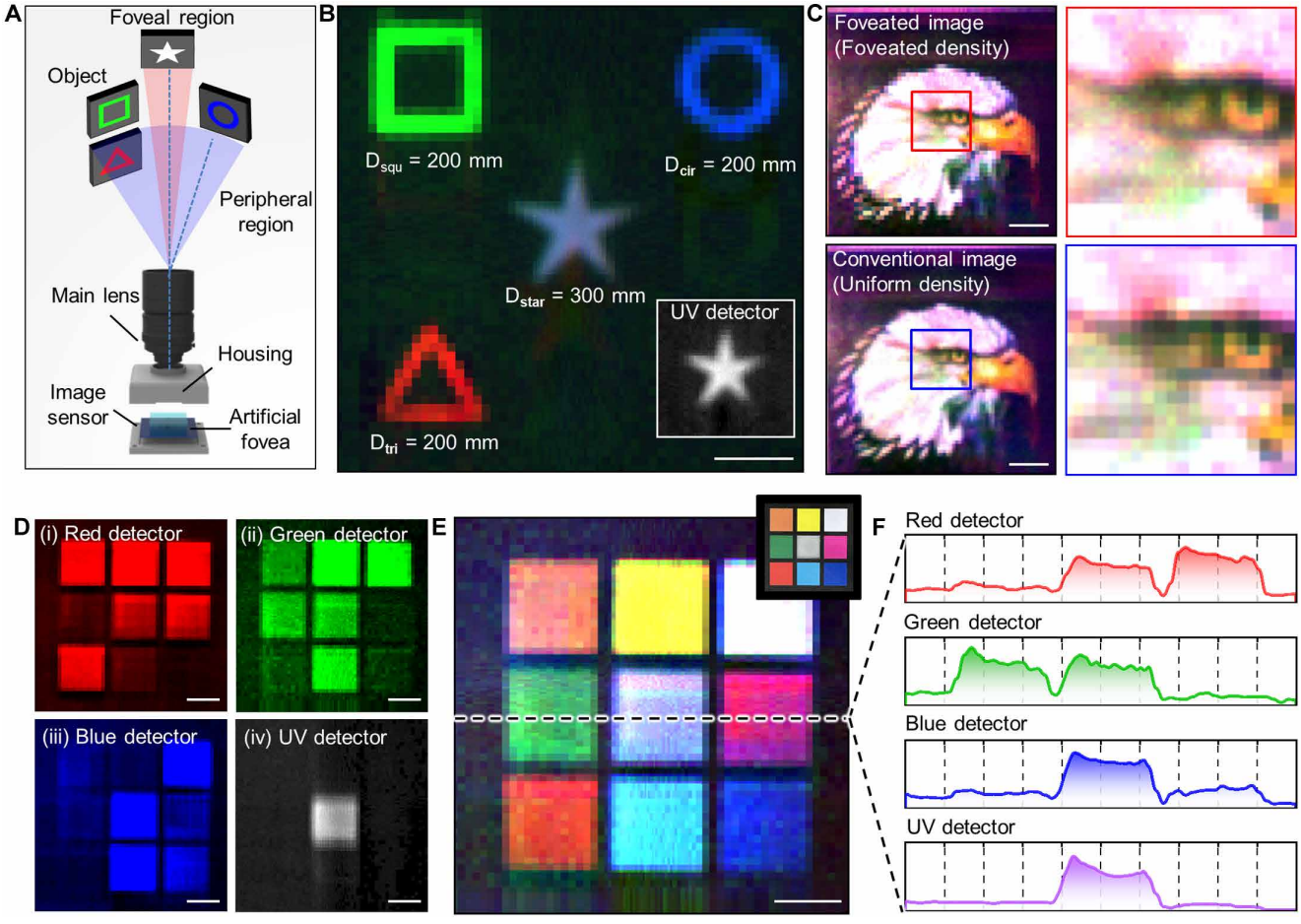

Fig. 5. Foveated and multispectral imaging demonstration using the avian-eye-inspired perovskite artificial vision system. (**A**) Schematic illustration of the measurement setup for the imaging demonstration. Four objects (triangle, square, circle, and star shape) were placed at two different distances ($D_{tri} = D_{squ} = D_{cir} = 200$ mm and $D_{star} = 300$ mm). (**B**) Imaging demonstration of the foveated and multispectral vision. The inset shows the star-shaped image obtained from UV detector. Scale bar, 2 mm. (**C**) Imaging demonstration using the multispectral image sensor with foveated density and uniform density. The object distance is 200 mm. Scale bars, 2 mm. (**D**) Colored images obtained from each detector of the multispectral image sensor. The object distance is 200 mm. Scale bars, 2 mm. (**E**) Reconstructed image by combining color information obtained from each detector of the multispectral image sensor. The inset shows an optical camera image of the object. Scale bar, 2 mm. (**F**) Graph of the intensity profiles obtained from reconstructed image [indicated by a dashed line in (E)].

the simulation results (Fig. 4, F and G, and fig. S15, A to C), foveated imaging yielded a clear and high-resolution image in the central region, whereas a hawk's eye image exhibited a diminished resolution when the pixel density was uniformly distributed (fig. S15, D to F).

Subsequently, the multispectral imaging capabilities were tested using a color checker containing diverse colors (R, G, B, yellow, magenta, cyan, orange, white, and UV). To facilitate imaging of these various colors, the color checker was illuminated with a white LED, and the reflected light from the color checker was used as the light source (fig. S16). Figure 5D illustrates the color information experimentally acquired from each photodetector in the artificial vision system that successfully extracted R, G, B, and UV information without color filters. By blending this color information, a reconstructed color image could be derived (Fig. 5E). To verify the accuracy of the color information, a comparison between the color obtained from a mobile phone camera (iPhone 14, Apple Inc.) and the color of the reconstructed image was made in the International Commission on Illumination 1931 color space (fig. S17). The colors of the reconstructed image were well represented without chromatic aberration and also corresponded well with the original colors of the color checker. (Fig. 5E, inset; fig. S18; table S1; and see the "Optical simulation showing chromatic aberration in the artificial fovea" section in Supplementary Methods). Figure 5F presents the cross-sectional intensity profile derived from the reconstructed image in the dashed line region of Fig. 5E. The profiles confirmed the presence of color information related to R, G, B, and UV, which match the color information of Fig. 5D.

Simulation study on the object and motion detection capability

Further imaging simulations were conducted under optimal conditions (such as high resolution and rapid frame rate) to assess the capabilities of the artificial fovea module in identifying objects and motion (movies S1 and S2 and figs. S19 and S20). The simulation for confirming the object recognition capability was performed by using the You Only Look Once (YOLO) version 5 algorithm on ray-traced

images with a video context where a car (target object) was centrally located and was being tracked by an uncrewed aerial vehicle (fig. S21A and movie S1). Figure 6 (A and B) displays the simulation results for the first frame extracted from movie S1. In the original image, the object (car) at the center was not magnified, resulting in a low confidence score of 0.39 (Fig. 6A). However, when using the foveated vision facilitated by the artificial fovea module, the object was magnified, resulting in a high confidence score of 0.76, which is approximately two times higher than that of the original image (Fig. 6B). Figure 6C illustrates the confidence scores of the original image and foveated vision across frames 1 to 150, denoting that the artificial fovea enhanced object recognition efficiency.

The artificial fovea module also enhances sensitivity in detecting the object's motion (movie S2 and fig. S20). The optical flow was computed by executing a ray-tracing simulation on video frames depicting moving cars on a highway to substantiate the advances in motion detection capability (fig. S21B). For two consecutive frames subjected to ray tracing, the Farneback algorithm, a method based on dense distribution for optical flow computation (*59*), was used, and the magnitude of motion was visualized using arrows (Fig. 6, D and E). The arrows were more elongated in the foveated vision than in the original image, suggesting that the foveated vision is more proficient at detecting the object's motion. A quantitative analysis was also undertaken to verify the motion detection capability of the artificial fovea module (Fig. 6F). In the original image, the range of movement varied from 6 to 18 pixels, separated by gaps of 9 pixels. In contrast, foveated vision demonstrated a much wider span, extending roughly from 5 to 38 pixels, with 33-pixel intervals. As a consequence of this augmented span of movement fluctuations, the foveated vision showed the enhanced capability for motion detection by more than 3.6-fold.

DISCUSSION

In this work, we introduced an avian eye–inspired perovskite artificial vision system that mimics both structural and functional aspects of the avian vision, enabling foveated and multispectral imaging. This system consisted of an artificial fovea and a multispectral image sensor. The architecture of the artificial fovea and the spatial allocation of the photodetector pixels were optimized via optical simulations to deliver foveated vision, enhancing the magnification of the target object. The system further incorporated vertically stacked perovskite photodetector arrays sensitive to various spectral ranges, facilitating the detection of RGB and UV colors without the need for color filters. The capabilities of the avian eye–inspired perovskite artificial vision system to provide foveated and multispectral imaging were validated through imaging demonstrations.

However, there are remaining challenges to be addressed for commercialization of this avian eye–inspired artificial vision. First, the detectivity and stability of the multispectral image sensor need to be improved. Optimization of perovskite films and device structures to suppress the internal and interfacial defects can reduce the dark current and increase detectivity and stability (*56*, *60*, *61*). The relatively low pixel resolution is the second issue. To address this issue, it is essential to study new patterning methods that can form high-resolution patterns and are compatible with a variety of materials (bulk film, nanoparticles, and nanowires) and device structures (photoresistor, photodiode, and phototransistor). Combined with these efforts to improve the current work, the advanced capabilities of this avian eye–inspired perovskite artificial vision system can be particularly advantageous for robotic vision, such as for uncrewed aerial vehicles and autonomous vehicles, given its specialization in detecting target objects and their motion.

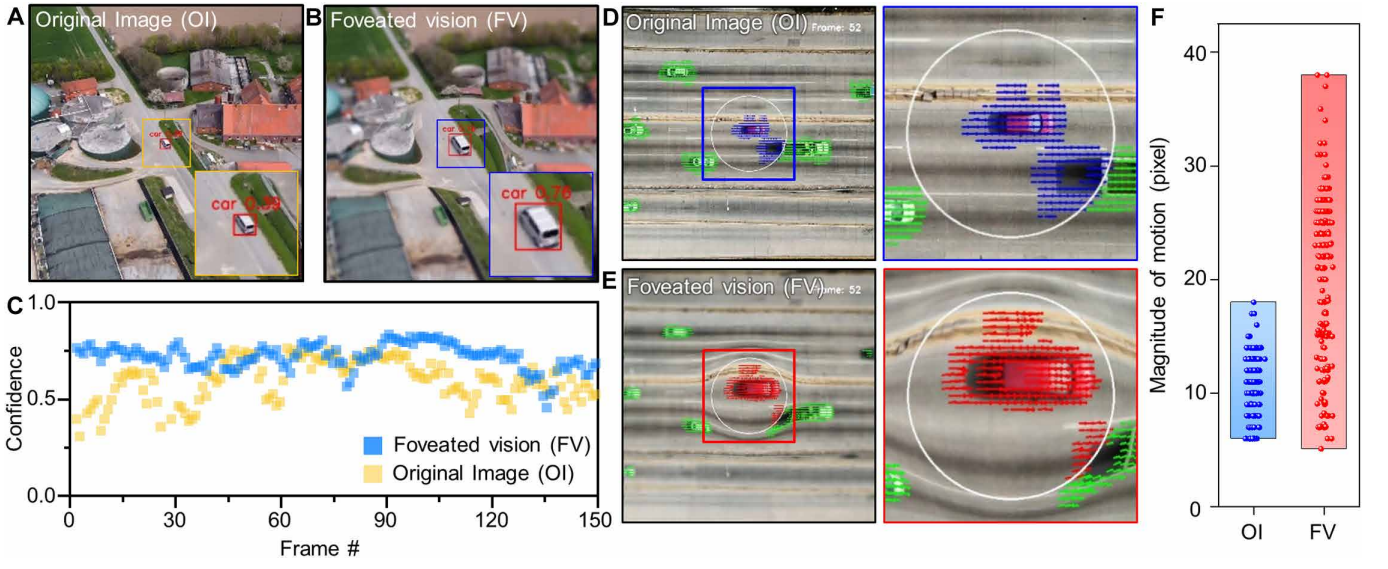

Fig. 6. Object/motion detection capabilities of the avian eye–inspired artificial vision system. (**A** and **B**) Simulation results showing object recognition capability of the original image (A) and foveated vision (B) based on YOLO v5. (**C**) Scatter plot of confidence for foveated vision and original image during 150 frames. (**D** and **E**) Simulation results showing the motion detection capability of the original image (D) and foveated vision (E) with optic flow based on the Farneback algorithm. The white circle presents the image center, and the arrow depicts visualized motion. (**F**) Scatter plot of the magnitude of motion within the center of images for the 52nd frame [indicated by white circles in (D) and (E)].

MATERIALS AND METHODS

Materials

All materials were used as purchased unless otherwise specified. A silicon dioxide wafer was purchased from SK Siltron. Methylammonium iodide, methylammonium bromide, methylammonium chloride, formamidinium iodide, formamidinium bromide, and formamidinium chloride were purchased from Greatcell Solar. PbI_2 (99.999%), $PbBr_2$ (99.999%), and $PbCl_2$ (99.999%) were purchased from Alfa Aesar. Poly(pyromellitic dianhydride-co-4,4′-oxydianiline), amic acid solution [polyimide (PI)], *N*,*N*′-dimethylformamide, dimethyl sulfoxide, and chlorobenzene were purchased from Sigma-Aldrich. Poly(methyl methacrylate) was purchased from Kayaku Advanced Materials. Polydimethylsiloxane (PDMS) was purchased from Dow Corning Corporation.

Optical simulation for artificial fovea module

The structure of the artificial fovea was conceptualized and fine-tuned using a Monte Carlo–based ray-tracing program (Optics studio 2023, radiant Zemax). The main lens was based on a Zemax model of a conventional lens with a 35-mm focal length (86573, Edmund Optics). The design of the artificial fovea involved generating its outline with numerical software (MATLAB 2016a, MathWorks, Inc.), followed by using a commercial computer-aided design tool to render it into an stereolithography file intended for optical simulation. The overall configuration of the optical system used in the simulation is presented in table S2. The distance between the object and the main lens was modulated between 150 and 450 mm to facilitate the simulation and calculate the RMS spot radii for the image simulation. At the same time, the angle of the incident field was varied from 0° to 8°. The dimensions of the image plane were established as 16 mm by 16 mm, and the pixel count for the image simulation was set at 1000 pixels by 1000 pixels.

Fabrication of artificial fovea

The artificial fovea was fabricated by demolding a clear elastomer (PDMS, SYLGARD 184) mixed with a curing agent in a ratio of 10:1 (fig. S3). The mold was manufactured using acrylonitrile butadiene styrene–like material through the stereolithography three-dimensional (3D) printing method. The elastomer was degassed in a vacuum chamber to remove air bubbles and to ensure optical functionality. As an anti-adhesive spray, a fluorocarbon mold release agent (DAIFREE GA-7550, Daikin, Japan) was applied to the mold's surface. Subsequently, the elastomer was poured into the 3D-printed mold, and the surface was covered to produce a flat surface. Curing of the elastomer was achieved in a convection oven at 60°C for more than 8 hours.

Optical simulation for optimization of perovskite layers

The optimization of the perovskite layers was carried out using rigorous coupled wave analysis (RCWA) facilitated by commercial software (DiffractMod, RSoft Design Group). The refractive index (n) and extinction coefficient (k) of the perovskite layers were ascertained by using ellipsometry measurement (Elli-SE-U, Ellipsotech). By using these quantified n and k values, the transmittance, absorbance, and reflectance of each perovskite layer were computed. To investigate the absorption capabilities of the perovskite layers at varying thicknesses, RCWA simulations were implemented, adjusting the thickness from 0.2 to 1.0 μm. The absorption position associated with each wavelength was analyzed for the vertically stacked perovskite layers. The "rand" function in MATLAB was used to create a variety of random surfaces with different roughnesses from 0 to 20%. The total thickness (t_{total}) of the perovskite layer was set to 1 μm, and the amplitude of the thickness (t_{amp}) was defined by multiplying t_{total} by the roughness.

Fabrication of perovskite photodetector arrays

The silicon dioxide wafer was washed with piranha solution and treated with UV-ozone for 15 min. Then, PI (15 weight %) was spin-coated at 8000 rpm for 60 s and annealed at 180°C for 30 min and 250°C for 2 hours under ambient conditions. Indium tin oxide (50 nm) was deposited by sputtering (35 W, 0.005 torr, and 275°C) and patterned to form interdigitated electrodes. After that, chromium (Cr) (10 nm) and gold (Au) (100 nm) layers were sequentially deposited by thermal evaporation under high vacuum ($<\sim10^{-6}$ torr) and patterned to form electrodes. An epoxy layer (SU-8 2, MicroChem) was coated and patterned on the substrate through photolithography to prevent contact between the Cr/Au and aluminum (Al) interconnection lines. Then, it was hard-baked at 150°C for 15 min. Al was deposited using an electron beam evaporator under high vacuum ($< \sim10^{-6}$ torr) and patterned through a lift-off process to form interconnection lines. A negative photoresist (AZ 2070, MicroChem) was used in the lift-off process. Then, the perovskite film was patterned by the previously reported swelling-induced lift-off method (*52*). The perovskite precursor solutions for the four types of photodetector arrays were prepared according to table S3. The perovskite precursor solutions were spin-coated at 3000 rpm for 30 s. During the spin-coating process, 500 μl of chlorobenzene was dropped onto the substrate 10 s before the end of coating. Subsequently, the substrates were annealed at 110°C for 1 hour. Preparation and patterning of perovskite films were performed in a glove box filled with argon gas [$O_2 < 1$ parts per million (ppm), $H_2O < 1$ ppm] to prevent damage from oxygen and moisture.

Transfer printing process for the multispectral image sensor

PDMS was mixed with the curing agent at a ratio of 40:1. Then, the PDMS mixture was diluted by mixing with *tert*-butanol (1:2, w/w). The diluted PDMS solution, which acts as an encapsulation layer and an adhesive layer, was spin-coated at 3000 rpm for 120 s. In this process, thermal release tape (TRT) was used to mask the contact electrodes of each photodetector array, and then it was removed on a hotplate at 110°C. Each photodetector array, peeled off from the donor substrate using TRT, was aligned and transferred using a mask aligner (MDA-400 M, MIDAS System). The transfer was completed by removing the TRT on a hotplate at 110°C. This transfer printing process was repeated three times to transfer G, B, and UV detectors.

Perovskite layers and device characterization and measurement

All measurements were performed under ambient conditions. XRD patterns were measured with a diffractometer (SmartLab, Rigaku) using Cu Kα radiation ($\lambda = 1.54$ Å). Steady-state PL spectra of the four types of perovskite layers were measured at room temperature in the ambient air using a LabRAM HR Evolution (HORIBA). The excitation wavelength for PL is 325 nm. The transmittance and absorbance spectra were measured using a UV-Vis-NIR spectrometer (Cary 5000, Varian). A cross-sectional scanning electron microscope (SEM) image of the multispectral image sensor was measured using a cryo–field emission SEM (Crossbeam 550, Carl Zeiss). Spectral

responsivity was measured using an IQE-200B quantum efficiency measurement system (Newport) under ambient conditions and −3-V bias. Different LEDs (MWWHL, Thorlab) with wavelengths of 365, 470, 530, and 625 nm were used as light sources for photoresponse measurements. A power meter (PM100D, Thorlabs) equipped with a photodiode power sensor (S120VC, Thorlabs) was used to measure the light intensities of the LEDs. The electrical characteristics of individual pixels were measured using a semiconductor device analyzer (B1500A, Agilent) and a probe station (MST-5500B, MSTECH). A waveform generator was used to chop light into square wave optical signals (33511B, Agilent).

Imaging demonstration of the avian eye–inspired artificial vision

A custom measurement setup was used to demonstrate the foveated and multispectral imaging capabilities of the avian eye–inspired artificial vision (figs. S12, S14, S22, and S23). Five LEDs (M365L3, M470L5, M530L4, M625L4, and MWWHL, Thorlab), each emitting distinct wavelengths (365, 470, 530, and 625 nm, and white), served as the light sources. To execute scanning measurements, a motor-driven linear translation stage (CMA-12CCCL, Newport), complemented by a precision motor controller (ESP301, Newport), was used to secure the multispectral image sensor (fig. S22). The data acquisition (DAQ) process involved capturing frames at 0.2-mm intervals while moving 2 mm in both the x and y directions. A customized DAQ board was used to collect pixel data from each color channel in an 8 pixel–by–8 pixel array; this board consisted of an analog-to-digital converter and a field programmable gate array chip (fig. S23). The multispectral image sensor was connected to the DAQ board using an anisotropic conductive film. To control the motorized linear stage and acquire photocurrent information from the image sensor, a programmable software (MATLAB R2016a, MathWorks Inc.) was used. For the multispectral imaging display, two unique objects were crafted: one reflecting light and another semitransparent version designed to emulate UV light. To achieve semitransparency, a diffusion film (LDL90DF, LX Hausys, Korea) was affixed to the object (fig. S24). The pixelated images obtained from each color channel were postprocessed to generate reconstructed color images and intensity equalization (fig. S25).

Statistical analysis

SEs in Fig. 3F ($n = 10$ for each detector) and fig. S8 (C to F) ($n = 5$ for each detector) were calculated using Excel. Fitted line plots in fig. S10 (A to D) were made using OriginPro 8.5.

Supplementary Materials

This PDF file includes:

Methods
Figs. S1 to S25
Tables S1 to S3

Other Supplementary Material for this manuscript includes the following:

Movies S1 and S2

REFERENCES AND NOTES

1. M. S. Kim, J.-E. Yeo, H. Choi, S. Chang, D.-H. Kim, Y. M. Song, Evolution of natural eyes and biomimetic imaging devices for effective image acquisition. *J. Mater. Chem.* **11**, 12083–12104 (2023).
2. G. J. Lee, C. Choi, D. H. Kim, Y. M. Song, Bioinspired artificial eyes: Optic components, digital cameras, and visual prostheses. *Adv. Funct. Mater.* **28**, 1705202 (2018).
3. M. S. Kim, M. S. Kim, G. J. Lee, S. H. Sunwoo, S. Chang, Y. M. Song, D. H. Kim, Bio-inspired artificial vision and neuromorphic image processing devices. *Adv. Mater. Technol.* **7**, 2100144 (2022).
4. J. Chen, Z. Zhou, B. J. Kim, Y. Zhou, Z. Wang, T. Wan, J. Yan, J. Kang, J.-H. Ahn, Y. Chai, Optoelectronic graded neurons for bioinspired in-sensor motion perception. *Nat. Nanotechnol.* **18**, 882–888 (2023).
5. F. Liao, Z. Zhou, B. J. Kim, J. Chen, J. Wang, T. Wan, Y. Zhou, A. T. Hoang, C. Wang, J. Kang, J.-H. Ahn, Y. Chai, Bioinspired in-sensor visual adaptation for accurate perception. *Nat. Electron.* **5**, 84–91 (2022).
6. Y. Hu, H. Yang, J. Huang, X. Zhang, B. Tan, H. Shang, S. Zhang, W. Feng, J. Zhu, J. Zhang, Y. Shuai, D. Jia, Y. Zhou, P. A. Hu, Flexible optical synapses based on In2Se3/MoS2Heterojunctions for artificial vision systems in the near-infrared range. *ACS Appl. Mater. Interfaces* **14**, 55839–55849 (2022).
7. L. Gu, S. Poddar, Y. Lin, Z. Long, D. Zhang, Q. Zhang, L. Shu, X. Qiu, M. Kam, A. Javey, Z. Fan, A biomimetic eye with a hemispherical perovskite nanowire array retina. *Nature* **581**, 278–282 (2020).
8. Y. Kim, C. Zhu, W.-Y. Lee, A. Smith, H. Ma, X. Li, D. Son, N. Matsuhisa, J. Kim, W.-G. Bae, S. H. Cho, M.-G. Kim, T. Kurosawa, T. Katsumata, J. W. F. To, J. Y. Oh, S. Paik, S. J. Kim, L. Jin, F. Yan, J. B.-H. Tok, Z. Bao, A hemispherical image sensor array fabricated with organic photomemory transistors. *Adv. Mater.* **35**, e2203541 (2023).
9. Z. Rao, Y. Lu, Z. Li, K. Sim, Z. Ma, J. Xiao, C. Yu, Curvy, shape-adaptive imagers based on printed optoelectronic pixels with a kirigami design. *Nat. Electron.* **4**, 513–521 (2021).
10. Z. Long, X. Qiu, C. L. J. Chan, Z. Sun, Z. Yuan, S. Poddar, Y. Zhang, Y. Ding, L. Gu, Y. Zhou, W. Tang, A. K. Srivastava, C. Yu, X. Zou, G. Shen, Z. Fan, A neuromorphic bionic eye with filter-free color vision using hemispherical perovskite nanowire array retina. *Nat. Commun.* **14**, 1972 (2023).
11. C. Choi, M. K. Choi, S. Liu, M. S. Kim, O. K. Park, C. Im, J. Kim, X. Qin, G. J. Lee, K. W. Cho, M. Kim, E. Joh, J. Lee, D. Son, S.-H. Kwon, N. L. Jeon, Y. M. Song, N. Lu, D.-H. Kim, Human eye-inspired soft optoelectronic device using high-density MoS2-graphene curved image sensor array. *Nat. Commun.* **8**, 1664 (2017).
12. L. Gu, M. M. Tavakoli, D. Zhang, Q. Zhang, A. Waleed, Y. Xiao, K.-H. Tsui, Y. Lin, L. Liao, J. Wang, Z. Fan, 3D Arrays of 1024-pixel image sensors based on lead halide perovskite nanowires. *Adv. Mater.* **28**, 9713–9721 (2016).
13. K. Zhang, Y. H. Jung, S. Mikael, J.-H. Seo, M. Kim, H. Mi, H. Zhou, Z. Xia, W. Zhou, S. Gong, Z. Ma, Origami silicon optoelectronics for hemispherical electronic eye systems. *Nat. Commun.* **8**, 1782 (2017).
14. I. Jung, J. Xiao, V. Malyarchuk, C. Lu, M. Li, Z. Liu, J. Yoon, Y. Huang, J. A. Rogers, Dynamically tunable hemispherical electronic eye camera system with adjustable zoom capability. *Proc. Natl. Acad. Sci. U.S.A.* **108**, 1788–1793 (2011).
15. C. Choi, J. Leem, M. Kim, A. Taqieddin, C. Cho, K. W. Cho, G. J. Lee, H. Seung, H. J. Bae, Y. M. Song, T. Hyeon, N. R. Aluru, S. W. Nam, D.-H. Kim, Curved neuromorphic image sensor array using a MoS2-organic heterostructure inspired by the human visual recognition system. *Nat. Commun.* **11**, 5934 (2020).
16. M. Kim, G. J. Lee, C. Choi, M. S. Kim, M. Lee, S. Liu, K. W. Cho, H. M. Kim, H. Cho, M. K. Choi, N. Lu, Y. M. Song, D.-H. Kim, An aquatic-vision-inspired camera based on a monocentric lens and a silicon nanorod photodiode array. *Nat. Electron.* **3**, 546–553 (2020).
17. M. Lee, G. J. Lee, H. J. Jang, E. Joh, H. Cho, M. S. Kim, H. M. Kim, K. M. Kang, J. H. Lee, M. Kim, H. Jang, J.-E. Yeo, F. Durand, N. Lu, D.-H. Kim, Y. M. Song, An amphibious artificial vision system with a panoramic visual field. *Nat. Electron.* **5**, 452–459 (2022).
18. M. Kim, S. Chang, M. Kim, J.-E. Yeo, M. S. Kim, G. J. Lee, D.-H. Kim, Y. M. Song, Cuttlefish eye–inspired artificial vision for high-quality imaging under uneven illumination conditions. *Sci. Robot.* **8**, eade4698 (2023).
19. D. Floreano, R. Pericet-Camara, S. Viollet, F. Ruffier, A. Brückner, R. Leitel, W. Buss, M. Menouni, F. Expert, R. Juston, M. K. Dobrzynski, G. L'Eplattenier, F. Recktenwald, H. A. Mallot, N. Franceschini, Miniature curved artificial compound eyes. *Proc. Natl. Acad. Sci. U.S.A.* **110**, 9267–9272 (2013).
20. S. Thiele, K. Arzenbacher, T. Gissibl, H. Giessen, A. M. Herkommer, 3D-printed eagle eye: Compound microlens system for foveated imaging. *Sci. Adv.* **3**, e1602655 (2017).
21. Z. Ji, Y. Liu, C. Zhao, Z. L. Wang, W. Mai, Perovskite wide-angle field-of-view camera. *Adv. Mater.* **34**, e2206957 (2022).
22. Y. M. Song, Y. Xie, V. Malyarchuk, J. Xiao, I. Jung, K.-J. Choi, Z. Liu, H. Park, C. Lu, R.-H. Kim, R. Li, K. B. Crozier, Y. Huang, J. A. Rogers, Digital cameras with designs inspired by the arthropod eye. *Nature* **497**, 95–99 (2013).
23. K. Kim, K.-W. Jang, J.-K. Ryu, K.-H. Jeong, Biologically inspired ultrathin arrayed camera for high-contrast and high-resolution imaging. *Light Sci. Appl.* **9**, 28 (2020).
24. M. Garcia, C. Edmiston, T. York, R. Marinov, S. Mondal, N. Zhu, G. P. Sudlow, W. J. Akers, J. Margenthaler, S. Achilefu, R. Liang, M. A. Zayed, M. Y. Pepino, V. Gruev, Bio-inspired imager improves sensitivity in near-infrared fluorescence image-guided surgery. *Optica* **5**, 413–422 (2018).
25. A. Altaqui, P. Sen, H. Schrickx, J. Rech, J.-W. Lee, M. Escuti, W. You, B. J. Kim, R. Kolbas, B. T. O'Connor, M. Kudenov, Mantis shrimp–inspired organic photodetector for simultaneous hyperspectral and polarimetric imaging. *Sci. Adv.* **7**, eabe3196 (2021).

26. M. Garcia, C. Edmiston, R. Marinov, A. Vail, V. Gruev, Bio-inspired color-polarization imager for real-time in situ imaging. *Optica* **4**, 1263–1271 (2017).
27. D. Keum, K.-W. Jang, D. S. Jeon, C. S. H. Hwang, E. K. Buschbeck, M. H. Kim, K.-H. Jeong, Xenos peckii vision inspires an ultrathin digital camera. *Light Sci. Appl.* **7**, 80 (2018).
28. Z.-Y. Hu, Y.-L. Zhang, C. Pan, J.-Y. Dou, Z.-Z. Li, Z.-N. Tian, J.-W. Mao, Q.-D. Chen, H.-B. Sun, Miniature optoelectronic compound eye camera. *Nat. Commun.* **13**, 5634 (2022).
29. M. P. Jones, K. E. Pierce Jr., D. Ward, Avian vision: A review of form and function with special consideration to birds of prey. *J. Exot. Pet Med.* **16**, 69–87 (2007).
30. A. Bringmann, Structure and function of the bird fovea. *Anat. Histol. Embryol.* **48**, 177–200 (2019).
31. A. W. Snyder, W. H. Miller, Telephoto lens system of falconiform eyes. *Nature* **275**, 127–129 (1978).
32. R. J. Pumphrey, The theory of the fovea. *J. Exp. Biol.* **25**, 299–312 (1948).
33. G. L. Walls, *The Vertebrate Eye and Its Adaptive Radiation* (Cranbrook Institute of Science, 1942).
34. I. C. Cuthill, J. C. Partridge, A. T. D. Bennett, S. C. Church, N. S. Hart, S. Hunt, Ultraviolet vision in birds. *Adv. Stud. Behav.* **29**, 159–214 (2000).
35. C. Tedore, D.-E. Nilsson, Avian UV vision enhances leaf surface contrasts in forest environments. *Nat. Commun.* **10**, 238 (2019).
36. M. Mitkus, P. Olsson, M. B. Toomey, J. C. Corbo, A. Kelber, Specialized photoreceptor composition in the raptor fovea. *J. Comp. Neurol.* **525**, 2152–2163 (2017).
37. J. Honkavaara, M. Koivula, E. Korpimäki, H. Siitari, J. Viitala, Ultraviolet vision and foraging in terrestrial vertebrates. *Oikos* **98**, 505–511 (2002).
38. J. Rajchard, Ultraviolet (UV) light perception by birds: A review. *Vet. Med.* **54**, 351–359 (2009).
39. V. A. Tucker, The deep fovea, sideways vision and spiral flight paths in raptors. *J. Exp. Biol.* **203**, 3745–3754 (2000).
40. C. A. Curcio, K. R. Sloan, R. E. Kalina, A. E. Hendrickson, Human photoreceptor topography. *J. Comp. Neurol.* **292**, 497–523 (1990).
41. S. Panda-Jonas, J. B. Jonas, R. A. Jonas, Photoreceptor density in relation to axial length and retinal location in human eyes. *Sci. Rep.* **12**, 21371 (2022).
42. M. Mitkus, S. Potier, G. R. Martin, O. Duriez, A. Kelber, Raptor vision, in *Oxford Research Encyclopedia of Neuroscience* (Oxford Univ. Press, 2018).
43. B. Bayer, Color imaging array, US Patent No. 3971065 (1976).
44. W. Qarony, M. Kozawa, H. A. Khan, M. I. Hossain, A. Salleo, Y. H. Tsang, J. Y. Hardeberg, H. Fujiwara, D. Knipp, Vertically stacked perovskite detectors for color sensing and color vision. *Adv. Mater. Interfaces* **7**, 2000459 (2020).
45. B. He, C. Wang, B. Shi, L.-Y. Duan, Mop moire patterns using MopNet, in *Proceedings of the IEEE/CVF International Conference on Computer Vision* (IEEE, 2019), pp. 2424–2432.
46. D. N. Sidorov, A. C. Kokaram, Suppression of moire patterns via spectral analysis, in *Visual Communications and Image Processing 2002* (SPIE, 2002), pp. 895–906.
47. N. J. Jeon, J. H. Noh, Y. C. Kim, W. S. Yang, S. Ryu, S. I. Seok, Solvent engineering for high-performance inorganic–organic hybrid perovskite solar cells. *Nat. Mater.* **13**, 897–903 (2014).
48. G. E. Eperon, S. D. Stranks, C. Menelaou, M. B. Johnston, L. M. Herza, H. J. Snaitha, Formamidinium lead trihalide: A broadly tunable perovskite for efficient planar heterojunction solar cells. *Energ. Environ. Sci.* **7**, 982–988 (2014).
49. S. Prathapani, P. Bhargava, S. Mallick, Electronic band structure and carrier concentration of formamidinium–cesium mixed cation lead mixed halide hybrid perovskites. *Appl. Phys. Lett.* **112**, 092104 (2018).
50. B. Slimi, M. Mollar, I. B. Assaker, A. Kriaa, R. Chtourou, B. Marí, Synthesis and characterization of perovskite $FAPbBr_{3-x}I_x$ thin films for solar cells. *Monatshefte für Chemie-Chemical Monthly* **148**, 835–844 (2017).
51. S. Du, J. Yang, S. Qu, Z. Lan, T. Sun, Y. Dong, Z. Shang, D. Liu, Y. Yang, L. Yan, X. Wang, H. Huang, J. Ji, P. Cui, Y. Li, M. Li, Impact of precursor concentration on perovskite crystallization for efficient wide-bandgap solar cells. *Materials* **15**, 3185 (2022).
52. W. Lee, Y. J. Yoo, J. Park, J. H. Ko, Y. J. Kim, H. Yun, D. H. Kim, Y. M. Song, D.-H. Kim, Perovskite microcells fabricated using swelling-induced crack propagation for colored solar windows. *Nat. Commun.* **13**, 1946 (2022).
53. J. H. Koschwanez, R. H. Carlson, D. R. Meldrum, Thin PDMS films using long spin times or tert-butyl alcohol as a solvent. *PLOS ONE* **4**, e4572 (2009).
54. Y. Y. Kim, T. Y. Yang, R. Suhonen, A. Kemppainen, K. Hwang, N. J. Jeon, J. Seo, Roll-to-roll gravure-printed flexible perovskite solar cells using eco-friendly antisolvent bathing with wide processing window. *Nat. Commun.* **11**, 5146 (2020).
55. Z. Yan, T. Pan, M. Xue, C. Chen, Y. Cui, G. Yao, L. Huang, F. Liao, W. Jing, H. Zhang, M. Gao, D. Guo, Y. Xia, Y. Lin, Thermal release transfer printing for stretchable conformal bioelectronics. *Adv. Sci.* **4**, 1700251 (2017).
56. H. Zhu, S. Teale, M. N. Lintangpradipto, S. Mahesh, B. Chen, M. D. Mc Gehee, E. H. Sargent, O. M. Bakr, Long-term operating stability in perovskite photovoltaics. *Nat. Rev. Mater.* **8**, 569–586 (2023).
57. H. Yamamoto, Y. Yeshurun, M. D. Levine, An active foveated vision system: Attentional mechanisms and scan path covergence measures. *Comput. Vis. Image Underst.* **63**, 50–65 (1996).
58. S. J. Prince, J. H. Elder, Y. Hou, M. Sizintsev, Y. Olevskiy, Statistical cue integration for foveated wide-field surveillance, in *2005 IEEE Computer Society Conference on Computer Vision and Pattern Recognition (CVPR'05)* (IEEE, 2005), pp. 603–610.
59. G. Farnebäck, Two-frame motion estimation based on polynomial expansion, in *Image Analysis* (*13th Scandinavian Conference, SCIA 2003 Halmstad, Sweden, June 29–July 2, 2003 Proceedings 13*), J. Bigun, T. Gustavsson, Eds. (Springer, 2003), pp. 363–370.
60. R. Ollearo, J. Wang, M. J. Dyson, C. H. L. Weijtens, M. Fattori, B. T. van Gorkom, A. J. J. M. van Breemen, S. C. J. Meskers, R. A. J. Janssen, G. H. Gelinck, Ultralow dark current in near-infrared perovskite photodiodes by reducing charge injection and interfacial charge generation. *Nat. Commun.* **12**, 7277 (2021).
61. D. Wu, Y. Zhang, C. Liu, Z. Sun, Z. Wang, Z. Lin, M. Qiu, D. Fu, K. Wang, Recent progress of narrowband perovskite photodetectors: Fundamental physics and strategies. *Adv. Dev. Instrument.* **4**, 0006 (2023).

Acknowledgments: We are grateful to the reviewers for valuable and critical feedback on this manuscript. **Funding:** This research was supported by the Institute for Basic Science under grant numbers IBS-R006-A1 (to J.P., J.K., M.L. and D.-H.K.) and by Basic Science Research Program through the National Research Foundation of Korea (NRF) funded by the Ministry of Education (RS-2023-00276798 and RS-2023-00210438). This work was supported also by the National Research Foundation of Korea (NRF) funded by the Ministry of Science and ICT (2023R1A2C3004531) and by "Regional innovation mega project" program through the Korea Innovation Foundation funded by Ministry of Science and ICT (2023-DD-UP-0015). **Author contributions:** J.P., M.S.K., J.K., D.-H.K., and Y.M.S. conceptualized this work. J.P., M.S.K., J.K., S.C., M.L., G.J.L., D.-H.K., and Y.M.S. designed the experiments and analyzed the data. J.P., M.S.K., D.-H.K., and Y.M.S. wrote the paper. J.P. and J.K. fabricated the perovskite photodetector arrays and performed characterization of individual devices. M.S.K. and S.C. fabricated the artificial fovea and performed theoretical analysis on optics. All authors discussed the results and commented on the manuscript. **Competing interests:** The authors declare that they have no competing interests. **Data and materials availability:** All data needed to evaluate the conclusions in the paper are present in the paper or the Supplementary Materials. The data for this study have been deposited in the Dryad database (https://doi.org/10.5061/dryad.dv41ns263).

Submitted 6 September 2023
Accepted 26 April 2024
Published 29 May 2024
10.1126/scirobotics.adk6903

Science Robotics

Avian eye–inspired perovskite artificial vision system for foveated and multispectral imaging

Jinhong Park, Min Seok Kim, Joonsoo Kim, Sehui Chang, Mincheol Lee, Gil Ju Lee, Young Min Song, and Dae-Hyeong Kim

Sci. Robot. **9** (90), eadk6903. DOI: 10.1126/scirobotics.adk6903

Editor's summary

The eyes of certain bird species contain deep central foveae that can magnify a target object for motion tracking as well as four cone types corresponding to red, green, blue (RGB), and ultraviolet (UV) light. Inspired by these avian eyes, Park *et al.* developed an artificial vision system for foveated and multispectral imaging. The system was composed of an artificial Gaussian-shaped fovea that could magnify and focus an object similarly to a zoom lens and a vertically stacked perovskite photodetector array that could detect R, G, B, and UV light without filters. This vision system is particularly promising in uncrewed aerial vehicles for detecting target objects and their motion. —Melisa Yashinski

Science Robotics (ISSN 2470-9476) is published by the American Association for the Advancement of Science. 1200 New York Avenue NW, Washington, DC 20005. The title *Science Robotics* is a registered trademark of AAAS.